# Controlling protein nanocage assembly with

# hydrostatic pressure

*Kristian Le Vay[1,2], Ben M. Carter[3], Daniel W. Watkins[1], T-Y. Dora Tang[1], Valeska P. Ting[4], Helmut Cölfen[5], Robert P. Rambo[6], Andrew J. Smith[6], J. L. Ross Anderson\*[1,7], Adam W. Perriman\*[3]*

[1]School of Biochemistry, University of Bristol, University Walk, Bristol, BS8 1TD, UK.

[2]Bristol Centre for Functional Nanomaterials, HH Wills Physics Laboratory, University of Bristol, Tyndall Avenue, Bristol, BS8 1TL, UK.

[3]School of Cellular and Molecular Medicine, University of Bristol, University Walk, Bristol, BS8 1TD, UK.

[4]Bristol Composites Institute (ACCIS), University of Bristol, Queen's Building BS8 1TR, UK

[5]Department of Chemistry, University of Konstanz, Universitätsstraße 10, 78457 Konstanz, Germany

[6]Diamond Light Source Ltd., Diamond House, Harwell Science and Innovation Campus, Fermi Ave, Didcot OX11 0DE, UK

[7]BrisSynBio Synthetic Biology Research Centre, Life Sciences Building, University of Bristol, Tyndall Avenue, Bristol, BS8 1TQ, UK.

*Email: ross.anderson@bristol.ac.uk, chawp@bristol.ac.uk

23 **Controlling the assembly and disassembly of nanoscale protein cages is**

24 **fundamental to the internalisation of protein and non-proteinaceous**

25 **components for diverse bionanotechnological applications. To this end, here**

26 **we study the reversible, pressure-induced dissociation of a natural protein**

27 **nanocage, *E. coli* bacterioferritin (Bfr), principally using synchrotron radiation**

28 **small angle X-ray scattering and circular dichroism. We demonstrate that**

29 **hydrostatic pressures of 450 MPa are sufficient to completely dissociate the Bfr**

30 **icositetramer into protein dimers, and the reversibility and kinetics of the**

31 **reassembly process can be controlled by selecting appropriate buffer**

32 **conditions. We also demonstrate that the heme B prosthetic group present at**

33 **the subunit dimer interface influences the stability and pressure lability of the**

34 **cage, despite its location being discrete from the inter-dimer interface that is**

35 **key to cage assembly. This indicates a major cage-stabilising role for heme**

36 **within this family of ferritins.**

37

38 Nanoscale protein cages are exceptionally attractive scaffolds for bionanotechnology

39 and materials science, where they can be exploited as platforms for constructing

40 robust and configurable therapeutic delivery vectors[1], vaccines[2], nanoreactors[3,4] and

41 templates for the synthesis of diverse nanomaterials[5–8]. These multifunctional

42 containers, both natural[9–13] and designed[14,15], offer unparalleled control over size,

43 shape, microenvironment, surface functionalisation and stability when constructing

44 novel bionanomaterials.

45

46 The ability to control the assembly of such nanocages is an invaluable tool in the

47 synthesis of complex materials, and can be instrumental in facilitating the

48    encapsulation of non-native nanomaterials. While this can be achieved by exploiting

49    natural[16–18] or engineered[19–21] cage metastability, the use of such nanocages could

50    ultimately compromise the robustness of the final assembled material. For nanocages

51    with higher relative stability, harsher environmental conditions[22,23] are required that

52    can adversely affect the protein cage, its functional modifications or the intended

53    payload for encapsulation. New methods are therefore required to circumvent the

54    necessity for harsh chemical conditions or specific interfacial engineering to promote

55    cage instability, and to realise the full potential of these cages in bionanotechnology.

56

57    Here we report on how hydrostatic pressure can be employed to control the

58    disassembly and reassembly of the protein nanocage bacterioferritin from *E. coli* (Bfr).

59    While hydrostatic pressure has been previously employed to dissociate the weakly

60    stable cage-like assemblyHSP26[24], the structure is not truly hollow[25]. There are

61    currently no reports of complete, reversible hydrostatic pressure-induced dissociation

62    in a highly robust nanocage such as ferritin[26,27]. While hydrostatic pressure has been

63    applied to human ferritin to facilitate the loading of doxorubicin and increase protein

64    recovery[27], the assembly/disassembly of the cage under pressure was not

65    investigated. Specifically, we use synchrotron radiation small angle X-ray scattering[28]

66    to show that the Bfr nanocage dissociates reversibly under pressure, and that the

67    reassembly can be controlled by altering solution conditions. Hydrostatic pressures of

68    450 MPa were sufficient to induce reversible dissociation of the Bfr icositetramer into

69    subunit dimers, and the reversibility of the pressure-induced dissociation was found to

70    be highly dependent on ionic strength and temperature, allowing for control of

71    oligomerisation state through pressurisation and selection of buffer conditions.

72    Furthermore, we demonstrate that the pressure lability of the nanocage can be

73  modulated by removal of the native heme B prosthetic group. Our study exploits the

74  ability of SAXS to probe the quaternary, tertiary and secondary structure of proteins,

75  and will provide not only the means for studying the supramolecular assembly of these

76  highly valuable nanocages, but will also inform future methodologies for controlling

77  protein nanocage assembly for efficient payload encapsulation.

78

79  **Results & Discussion**

80  We initially probed the pressure-induced dissociation of the core-free, or apo-,

81  bacterioferritin icositetramer (ABfr) by gradually raising the applied hydrostatic

82  pressure in a diamond-windowed SAXS pressure cell to 450 MPa in 25 MPa

83  increments, equilibrating for 40 seconds prior to data collection at each pressure. An

84  oscillating scattering pattern was observed at low pressures (Figure 1a), characteristic

85  of the hollow nanocage structure. With increasing pressure, fringes corresponding to

86  the hollow sphere form factor broaden and then disappear, indicating increasing

87  polydispersity and decreasing concentration of icositetramer due to dissociation into

88  lower order oligomeric species. The presence of isosbestic points in the reciprocal

89  space and Kratky data (Figure 1a and 1b), indicate that two species contribute to I($q$)

90  with proportional stoichiometry. At higher pressures (> 300 MPa), a slight drift in the $q$

91  value of the isosbestic points is observed, suggesting additional species likely

92  contribute to the dissociation process.

93

94  From the pair distance distribution factor (*P(r)*), we determined *I(0)* and the radius of

95  gyration, $R_g$ (Figure 1c), finding that the latter decreases non-linearly from 50 Å to 32

96  Å over the pressures applied here (Figure 1d). This non-linear change in $R_g$ with

97  pressure is due to the power law dependence of $R_g$ upon particle size, rather than

98    suggesting a cooperative dissociation mechanism. The data therefore indicate gradual

99    icositetramer dissociation with multiple intermediates, and a final state in which the

100   majority of species are small subunit oligomers. The $P(r)$ distribution is  characteristic

101   of a hollow sphere until 250 MPa. The maximum of this distribution, $P(r)_{max}$, occurs at

102   $r = 84$ Å, corresponds to the distance between the cage center and the protein shell

103   and decreases steadily with pressure, indicating gradual loss of the icositetramer. At

104   high pressures, the magnitude at $r = 84$ Å  tends to zero and a new $P(r)_{max}$, emerges

105   at $r = 32$ Å, corresponding to a subunit oligomer of ABfr, previously masked by that of

106   the fully assembled cage.

107

108   Using a linear combination of theoretical SAXS data from various oligomeric

109   components, we were able to identify possible dissociation pathways[29,30]. Our

110   prediction of possible stable oligomers using the PISA (Proteins, Interfaces, Surfaces

111   and Assemblies)[31] tool returned only the subunit dimer and icositetramer as stable

112   states (Table S1). We then used single value decomposition to determine the number

113   of required components (Figure S1 and S2) from the pressure dissociation SAXS, and

114   constructed various models using oligomer structures derived from crystal structures

115   of the ABfr icositetramer (Table S2, Figure S3 and S4). Two component models

116   consisting of the icositetramer and a subunit oligomer provided the worst fits of the

117   dataset (Table S3), though of these, the model consisting of the icositetramer and

118   dimer best represented the data. Three component models generally provided better

119   representations of the dissociation dataset, and all models in which the dimer was the

120   lowest oligomeric state gave the best fit quality. Thus, in this pressure range, we

121   assigned the initial and final state as icositetramer and dimer. Ultimately, we found

122   that the data were best represented by models comprised of icositetramer, dimer and

123    an intermediate hexamer, octamer or dodecamer (Figure 1e). We acknowledge that

124    there is no justification for selecting a specific intermediate state based on these data

125    alone, and therefore refrain from doing so; the equivalence of the models and lack of

126    cooperativity suggests that a range of intermediate states are present during

127    dissociation. Although little work has been carried out on pressure-induced ferritin

128    dissociation, there are many studies detailing pH and denaturant-induced dissociation

129    and reassembly of mammalian ferritin[32–37]. The dissociation products and

130    mechanisms of reassociation observed are consistent with the results obtained here,

131    with dissociation to subunit dimer and reassociation *via* intermediate species including

132    tetramers, hexamers and octamers most commonly reported.

133

134    To assess the effect of pressure on the internal structure, secondary structure and

135    folding of ABfr, we used a combination of Kratky plot analysis and high pressure

136    synchrotron radiation circular dichroism (CD). At low pressure, the Kratky plots for ABfr

137    exhibit multiple bell shaped peaks at low $q$ and converge to the baseline at high $q$,

138    indicating a globular, spherical structure (Figure 1b). At high pressure, low $q$ peaks

139    decrease in intensity and become less distinct, whilst the high $q$ region diverges from

140    the baseline, indicating a partially folded internal structure above 375 MPa. This may

141    alter tertiary structure and interfacial interactions, destabilising the icositetramer

142    structure. We observed no significant change in the circular dichroism spectra

143    between 0.1 MPa and experimental limit of this technique, 200 MPa (Figure 1f), and

144    predicted structural composition *via* basis spectra remained constant (alpha helix =

145    0.99, beta sheet, 0.01)[38]. The CD data support the SAXS data in this pressure range,

146    and it is therefore likely that the observed changes in quaternary structure up to 375

147   MPa are due to the system shifting towards a lower volume state, rather than

148   significant perturbation of the ABfr secondary structure[39].

149

150   We then explored the reversibility of the pressure dissociation process. Initially, ABfr

151   in 45 mM sodium phosphate (NaPi) buffer was pressurised to 450 MPa and held for 5

152   minutes before pressure release (Figure 2a). An immediate depression in $R_g$ was

153   observed, and the hollow spherical structure was lost after 30 seconds. Fitting the

154   change in icositetramer volume fraction against time with a single exponential function

155   (Figure S5), the observed rate constant ($k_{diss}$) of dissociation was determined to be

156   $0.114 \pm 0.002$ s$^{-1}$. Almost complete reassembly occurred over 30 minutes following

157   depressurisation, as apparent from the recovery of the radius of gyration over time

158   (Figure 2a) and the hollow cage form of the P(r) function (Figure 2b). Again, fitting the

159   change in icositetramer volume fraction against time with a single exponential function

160   (Figure S7), the observed rate constant of reassociation ($k_{ass}$), was determined to be

161   $0.006 \pm 0.001$ s$^{-1}$ (Figure S5). Following reassociation, we noted that the final $R_g$ and

162   *I(0)* values were slightly lower than initial values (Figure 2a, b). To quantify the degree

163   of reassociation and to control for possible radiation damage or background mismatch,

164   a sample of ABfr was pressurised under identical conditions without SAXS

165   measurement. Analytical ultracentrifugation (AUC) before pressurisation (Figure 2c,

166   Table S4) demonstrated that ABfr is almost fully assembled as the icositetramer ($S_{20,}$

167   $_w$ = 15.76, MW = 424 kDa). Following pressurisation (t = 60 minutes), 94.3% of ABfr

168   was assembled in the icositetramer state ($S_{20, w}$ = 16.1, MW = 426 kDa), with the

169   remaining material present as the subunit dimer ($S_{20, w}$ = 3.53, MW = 44.5 kDa). TEM

170   imaging confirmed the presence of assembled ABfr cages before and after

171   pressurisation, with no apparent change in morphology (Figure 2d, e).

172

173    The rate of reassociation under these conditions appears slow, and is significantly

174    slower than the calculated dimer collisional frequency[40] ($f_{25°C}$ = 6.79 x10$^5$ S$^{-1}$ at 25˚C)

175    demonstrating unequivocally that reassembly is not diffusion limited. We then sought

176    to determine whether recovery from pressure induced conformational drift influenced

177    the kinetics of reassociation[41,42]. We assessed the degree of protein denaturation by

178    inspection of a normalised Kratky plot (Figure 2f), in which globular protein exhibits a

179    maximum value of 1.104 for $qR_g=\sqrt{3}$, whilst unfolded protein has a maximum value of

180    1.5-2[43]. This plot confirmed that the protein recovers almost immediately from the

181    denatured state after pressure release, so the process is unlikely to be refolding-

182    mediated.

183

184    The relatively slow rate of association may also be due to a kinetic barrier in the

185    association process which could arise from repulsive interactions between subunit

186    dimers. To determine the types of interaction dominant in this process, we explored

187    the effect of ionic strength and temperature on the nanocage reassembly, finding

188    strong correlation between these parameters and the rate and completeness of

189    nanocage reassembly (Figure 3, Table S5). We observed the most efficient

190    reassembly in high ionic strength sodium phosphate buffer (45 mM, 250 mM NaCl, pH

191    7; I = 373 mM)), with higher initial $R_g$ than the low ionic strength buffers and almost

192    complete reassembly at both 5 and 25 °C. In contrast, the assembly was notably

193    slower and less complete in lower ionic strength sodium phosphate buffer (pH 7, 45

194    mM; I = 123 mM) at both temperatures, with only gradual recovery of $R_g$ over the 1500

195    seconds of measurement. Most notably, the reassembly process in water was

196    significantly impaired at 25 °C, and was effectively arrested at 5 °C, with no

197   discernable increase in $R_g$ observed over 1500 seconds, indicating the presence of

198   only discrete subunit dimers within this timeframe. Given these data, we propose that

199   the reassembly of ABfr nanocages is likely driven by hydrophobic dispersion forces

200   while opposed by coulombic repulsion.

201

202   Similar ionic strength dependencies on nanocage reassembly were observed for the

203   naturally heme-free *E. coli* ferritin FtnA[44] following low pH-induced dissociation, and it

204   is likely that the origin of this effect lies at the interface between ferritin subunit dimers,

205   which associate to form the highly charged, carboxylate-rich ion channels at the C3

206   and C4 interfaces[45–47]. The increased degree and rate of reassembly with temperature

207   is a strong indication that assembly is entropically driven by the formation of weak

208   protein-protein interactions[48]. For oligomeric assemblies, the enthalpic contribution

209   ($\Delta H$) is generally small, because the strength of protein-water and water-water

210   interactions are similar. As such, increasing temperature decreases the Gibb's free

211   energy of association ($\Delta G^{ass}$ ) and favours assembly.

212

213   We also observed a greater degree of dissociation following pressurization at 5°C (5

214   minutes at 450 MPa) at all ionic strengths tested here; previous studies of pressure-

215   induced viral capsid dissociation have reported similar effects, and were attributed to

216   a strong entropic contribution to the free energy of association[49].  In these cases,

217   higher temperatures lower $\Delta G^{ass}$, promoting association in systems where entropic

218   contributions to the free energy dominate. Once the interfacial protein-protein

219   interactions (principally salt bridges and dispersion interactions) are broken and the

220   oligomers dissociate, dipole-dipole protein-water interactions are formed in their

221   place[49,50]. At high pressure, inherently shorter dipole interactions are favoured over

222    dispersion interactions due to the differential effect of compression on bond strength,

223    and dissociation occurs due to the increasing formation of protein-water interactions.

224    In addition, the hydration of hydrophobic surfaces is more favourable at high pressure,

225    as the ordered solvation shell is denser than the bulk solvent. Both similar and

226    contrasting behaviours have been reported for viral capsids under pressure. Silva *et*

227    *al.*[51,52] demonstrated that the 86-subunit bromegrass mosaic virus capsid undergoes

228    a reversible partial dissociation into dimers upon application of pressure (10 %

229    dissociation at 200 MPa). In contrast, the turnip yellow mosaic virus irreversibly

230    decapsidates rather than dissociates under pressure, resulting loss of RNA and

231    formation of a holed capsid, as the subunit interface contains few pressure sensitive

232    salt bridge and is rich in pressure insensitive hydrogen bonding interactions[53].

233

234    We subsequently investigated the ability of the native heme B prosthetic group to

235    modulate cage stability. Using a well-established procedure for tetrapyrrole extraction,

236    we removed heme B from an acidified water:2-butanone mixture and confirmed the

237    successful removal by UV/visible spectroscopy (Figure 4a)[54]. We next explored the

238    composition of oligomeric species in this apo-apo-Bfr (AABfr) by sedimentation

239    velocity analytical ultracentrifugation (SV-AUC, Figure 4b). In contrast to the heme

240    containing ABfr, the SV-AUC distribution reveals a mixture of assembled icositetramer

241    ($S_{(20, w)}$ = 15.85, MW = 427.1 kDa, 62.1%) and subunit dimer ($S_{(20, w)}$ = 2.97, MW =

242    34.7 kDa, 37.9%). The icositetramer peak is broadened, indicating greater

243    polydispersity and potentially incomplete assembly. We further characterized this

244    mixture of species by high-performance liquid chromatography-SAXS (HPLC-SAXS)

245    (Figure 4c), and observed scattering patterns consistent with both the assembled

246    icositetrameric nanocage ($R_g$ = 49.88 Å), and a smaller ellipsoidal or parallelepipedal

247     particle[55]. The extrapolated $R_g$ (22.21 Å) of the smaller particle is in good agreement

248     with that calculated for the subunit dimer (PDBID: 2VXI, $R_g$ = 21.16 Å)[56], and the Kratky

249     plot (Figure 4d) indicates a folded structure, although with a greater degree of disorder

250     than the AABfr icositetramer. We used bead modelling to analyse the SAXS data for

251     both the ABfr and AABfr icositetramers and found excellent agreement between the

252     hollow spherical models and the published Bfr crystal structure (Figure 4e)[56]. Similarly,

253     the bead model of the AABfr subunit dimer closely overlays with the crystal structure

254     of the AABfr dimer (PDBID: 4CVP)[57]. To further probe the effects of removing heme B

255     from the nanocages, we used circular dichroism spectroscopy to determine the

256     thermal stabilities of the Bfr samples. We found the denaturation midpoints of ABfr ($T_m$

257     = 68°C) and AABfr ($T_m$ = 58°C) in agreement with previously reported values[58,59],

258     confirming that removal of heme B has an overall destabilizing effect on the protein.

259     Comparison of the ABfr and AAbfr subunit dimer crystal structures reveals slight

260     secondary and tertiary structure differences that may impact the ability of the dimer to

261     assemble into the icositetramer (Figure S6). In particular, the position of the E helix is

262     shifted in the heme free protein; this helix lies at the tetramerization interface and is

263     essential for cage assembly (Figure S7)[60].

264

265     These data indicate that the binding of heme B not only leads to an increase in thermal

266     stability of the bulk Bfr protein, but it specifically stabilises the nanocage assembly.

267     While such increases in thermal stability induced through cofactor binding in heme-

268     proteins are widely reported, the bound cofactor's impact on cage stability and

269     assembly is unknown[61]. To determine the effect of heme B on the pressure stability of

270     Bfr, we pressurised AABfr to 450 MPa in 25 MPa increments, allowing time at each

271     step for equilibration before SAXS measurement (Figure 5a). We found the real space

272    distribution for ABfr at ambient pressure is representative of a mixture of assembled

273    icositetramers and smaller subunit oligomers, in good agreement with the SV-AUC

274    data described above (Figure 5b). The icositetramer nanocage structure visible in the

275    real space distribution is rapidly lost with applied pressure, whilst the final state

276    resembles a mixture of the subunit dimer and other lower order oligomers. The Kratky

277    plots demonstrate a less globular structure than ABfr at similar pressures, and do not

278    reveal any further unfolding over the pressure range (Figure 5c). The initial $R_g$ for

279    AABfr (42 Å) Is notably lower than that of ABfr (50 Å) due to the mixture of icositetramer

280    and dimer at ambient pressure. The $R_g$ remains constant until 175 MPa, then

281    deceases, reaching a plateau at 350 MPa, demonstrating that AABfr is significantly

282    less pressure stable than ABfr (Figure 5d). The final $R_g$ of 35 Å, was higher than that

283    of ABfr (32 Å), suggesting a dissociation endpoint with a different oligomeric state.

284

285   **Conclusions**

286   We have demonstrated here that hydrostatic pressure is a valuable method to control

287   and modulate the assembly, disassembly and oligomeric composition of the

288   bacterioferritin nanocage. It is highly likely that this methodology can be extended to

289   other protein nanocages, especially those stabilized primarily by hydrophobic

290   interactions. Since the method we report here is also gentle, tunable and not limited

291   to intrinsically metastable or mutationally compromised cages, more robust hybrid

292   materials tolerant of harsh environmental conditions are potentially accessible. Full

293   cage dissociation might also provide a route to higher loading ratios of therapeutic

294   molecules or larger payloads unable to traverse the protein cage, leading, for example,

295   to significantly improved synthetic routes to nanocage-based drug delivery vehicles.

296

297   Furthermore, we have also demonstrated that the heme B prosthetic groups

298   significantly enhance the Bfr nanocage stability. While it has been previously reported

299   that heme B facilitates electron transfer and iron release from the Bfr core, this can

300   occur in the absence of the prosthetic group and it is notable that heme B is absent in

301   many/most of the known ferritins. It therefore seems plausible that an additional major

302   role of heme B in Bfr is to stabilise the protein nanocage, thus enabling the retention

303   of the protein superstructure for iron mineralisation.

304

305    **Methods**

306    **Protein expression and purification**

307    Bacterioferritin expression was carried out in T7 express *E. coli* BL21 (DE3) cells using

308    a modified pUC119 plasmid, PGS281 as described in Andrews *et al*[62]. Cultures were

309    grown aerobically at 37 °C in LB media containing 34 µg mL$^{-1}$ carbenicillin. Flasks

310    were shaken for 24 hours at 200 rpm, before cultures were harvested by centrifugation

311    (10 minutes, 7277 ×g rcf). The pellets were washed then re-suspended in lysis buffer

312    (1.5 mM $KH_2PO_4$, 8 mM $Na_2HPO_4$, 150 mM NaCl, 3 mM KCl, pH 7).

313    Phenylmethylsulfonyl fluoride (PMSF) (1 mM) was added, and then cells were lysed

314    using a probe sonicator (3 × 20s, maximum amplitude). The crude extract was then

315    centrifuged (47808 ×g, 60 minutes). The supernatant was decanted, heated to 70 °C

316    for 15 minutes, then cooled and centrifuged (47808 ×g, 30 minutes). The supernatant

317    was concentrated using a centrifugal concentrator (MWCO = 50 kDa) to half the

318    original volume. The extract was purified by size exclusion chromatography using a

319    Sephadex S200 26/600 column equilibrated with lysis buffer at a flow rate of 2.3 mL

320    *per* minute. Bfr containing fractions were pooled, concentrated, and then further

321    purified by anion exchange chromatography using a Q-Sepharose FF column. The

322    target protein was eluted with a linear gradient of 0-0.3 M NaCl in histidine buffer (20

323    mM histidine.HCl, pH 5.5). The purified protein was dialysed in a solution of EDTA (10

324    mM) and DTT (5 mM) to remove the native core, forming ABfr.

325

326    **High pressure SAXS measurement**

327    Data collection was carried out at the I22 beamline, Diamond Light Source (DLS,

328    Harwell, UK), using a hydrostatic pressure cell with a maximum operation pressure of

329    500 MPa[28]. Samples were loaded into thin-wall polycarbonate capillaries (θ=2 mm),

330    which were then sealed with a rubber bung and two-part adhesive. The beam energy

331    was 18 keV ($\lambda = 0.69$ Å) to reduce absorption from the diamond windows and water in

332    the beam path. ABfr samples were prepared at a concentration of 5 mg mL$^{-1}$ in a range

333    of buffers and centrifuged (10 minutes, 16000 ×g) prior to measurement. The collection

334    time for individual measurements was between 6 and 60 s. Hydrostatic pressure

335    experiments were performed under both equilibrium and dynamic, time resolved

336    conditions. In the former, the pressure was raised in incremental steps allowing time

337    for equilibrium before measurement. The beam was blocked during equilibration to

338    prevent radiation damage. In dynamic experiments the sample was pressurised, held

339    at pressure, then returned to ambient pressure whilst measuring the time resolved

340    scattering pattern. Pressure jump experiments were conducted in which pressure was

341    increased rapidly to 450 MPa whilst measuring the time resolved scattering.

342

343    The data were collected using a Pilatus P3-2M detector. The sample to detector

344    distance was 6 m, providing a $q$-range of 0.008-0.52 Å$^{-1}$. The two-dimensional data

345    sets were reduced using DAWN[63]. Briefly, the $q$-axis was calibrated using with a silver

346    behenate standard data, then detector images were masked, radially averaged from

347    the beam centre and normalised to absolute intensity using a glassy carbon standard.

348    Background subtraction was carried out using a user-written python script (Figure S8

349    and S9) to account for background mismatch in the high-$q$ data region. This mismatch

350    resulted from the necessity of using different capillaries for sample and background,

351    and slight changes in cell and capillary position when changing samples. Whilst this

352    mismatch was generally low, systemic under-subtraction at low pressure and over-

353    subtraction at high pressure was present across data sets. The background

354    measurement was multiplied by a constant to align the high-$q$ region with that of the

355     sample. The median I($q$) of the region $q$ = 0.3-0.4 Å$^{-1}$ was determined for both sample

356     and background data. The background was then multiplied by a constant, $k$, such that

357     the corrected median I($q$) of the background was equal to the median I($q$) of the sample

358     minus a small constant, $A$. The scaling constant was therefore:

359

360    
$$k = \frac{I(q)_{sample} - A}{I(q)_{background}} \qquad q = 0.3 - 0.4 \,\text{Å}^{-1}$$

361     This method was effective in background matching the high-$q$ data region and

362     preventing over and under subtraction with $k$ = 1 x 10$^{-5}$. Example data corrections for

363     ABfr at 0.1 MPa and 200 MPa are shown in Figure S8. The background adjustment

364     results in lower overall I($q$) relative to the unprocessed data, but the shape of the

365     scattering curve is preserved. Artefacts resulting from Kossel lines are visible in the

366     data at 200 MPa at $q$ = 0.016 and 0.7 Å$^{-1}$ despite background subtraction. The effect

367     is most visible in the 2D detector image, shown in Figure S9. Kossel lines are observed

368     between 100-300 MPa in both background and sample images. The intensity of the

369     effect is pressure dependent, and line position is dependent on the orientation of the

370     diamond windows. Care was taken to repeat background measurements following

371     window changes. However, mismatched line intensity between sample and

372     background resulted in artefacts in the reduced data. The mismatch occurs due to the

373     pressure dependence of line intensity: whilst pressure control is accurate to 0.1 MPa

374     in this apparatus, slight pressure loss often occurs during measurement due to

375     leakage. Consequently, pressure differences between samples and background

376     measurements of up to 0.3 MPa are observed. Although visible in the data, the

377     artefacts are small and not expected to affect subsequent fitting and data analysis.

378     Parasitic scattering is present in some data sets, particularly where Kossel lines

379    intersect with the beam-stop (Figure S9 (200 MPa)). This effect is not effectively

380    removed by background subtraction, and manifests as aggregation-like scattering at

381    $q < 0.04$ Å$^{-1}$, which precludes the use of Guinier methods for the approximation of I(0)

382    and $R_g$, but does not affect the determination of these parameters from the indirect

383    Fourier transform of the data.

384

385    **Circular Dichroism**

386    Circular dichroism (CD) spectroscopy was used to determine the relative thermal

387    stabilities of ABfr and AABfr and to investigate the secondary structure of both

388    proteins. Solutions of ABfr or AABfr (0.5 g L$^{-1}$) were prepared in 45 mM sodium

389    phosphate buffer (pH 7). The far UV spectrum (190-260 nm) was measured at 25 °C,

390    then the temperature was increased in 3 degree increments allowing for equilibration

391    (300s) at each step. The helical content was measured by monitoring mean residue

392    ellipticity at $\lambda$= 222 nm. The thermal denaturation midpoint temperature was

393    determined using sigmoidal fits of the raw the [$\theta_{222\ nm}$] data and from the maxima in

394    first differential of the [$\theta_{222\ nm}$] data (Figure 4f). Secondary structure composition was

395    determined by linear combination of basis spectra using CAPITO[38].

396

397    **High pressure circular dichroism**

398    High pressure circular dichroism measurements were carried out at the B23 beamline,

399    Diamond Light Source (DLS, Harwell, UK), using a hydrostatic pressure cell with a

400    maximum operation pressure of 200 MPa[64]. Results obtained were processed using

401    CDApps and OriginLab. Secondary structure estimation from CD spectra was carried

402    out using the CAPITO CD analysis and plotting tool[38].

403

404 **Sedimentation velocity analytical ultracentrifugation**

405 Sedimentation velocity was measured in sodium phosphate buffer (45 mM NaPi, 250

406 mM NaCl, pH 7) using a Beckmann ProteomeLab XL-I at 20 $^\circ$ C and 24000 rpm. Data

407 were collected at a wavelength of 418 nm. Date file time stamps were corrected using

408 REDATE, and continuous sedimentation velocity coefficient (c(S)) distributions were

409 produced using SEDFIT. Buffer density and viscosity were measured using an Anton-

410 Paar rolling ball viscometer. The protein partial specific volume was calculated from

411 the primary sequence ($\tilde{v}$ = 0.736 cm$^3$ g$^{-1}$).

412

413 **PISA analysis of ABfr**

414 A bioinformatics approach was adopted in order to identify potential dissociation states

415 of ABfr under pressure. The Proteins, Interfaces, Structures and Assemblies (PISA)

416 tool was used to calculate overall solvent accessible surface areas, solvation free

417 energies ($\Delta G^{int}$) and dissociation free energies ($\Delta G^{diss}$) for stable subunit oligomers of

418 ABfr[31,65,66]. The PISA analysis identifies thermodynamically stable assemblies of

419 subunits based on interfacial interactions. For ABfr, only the fully assembled

420 icositetramer and dimer were identified as stable quaternary structures in solution. The

421 surface areas and free energies of these species are shown in Table S1. The free

422 energy of dissociation, $\Delta G^{diss}$, corresponds to the free energy difference between

423 associated and dissociated states. A positive value indicates that the assembled state

424 is stable under standard conditions.

425

426 **SVD reconstruction of ABfr equilibrium pressure dissociation.**

427 SVDPLOT and Ultrascan II were used to produce a set of basis eigenvectors and

428 eigenvalues for the ABfr dataset (Figure S1)[67]. A non-parameterised runs test was

429    used to identify non-random curves in the eigenvector set[68]. Eigenvectors with $p <$

430    0.05 were deemed to be non-random, yielding 12 significant eigenvectors. Inspection

431    of the ABfr eigenvectors revealed that those with the highest two eigenvalues are

432    smooth curves reminiscent of scattering form factors, and so are likely to contain

433    structural information corresponding to the initial icositetramer and oligomeric

434    dissociation products. The subsequent curves are structured but contain significant

435    noise, and may contain contributions from minor species as well as background

436    components due to imperfect background subtraction. The data were then

437    reconstructed incrementally by adding eigenvectors to the model in order of

438    decreasing significance. The root mean squared deviation between the reconstructed

439    datasets and the experimental curves was calculated at each stage (Figure S2).

440

441    **Acknowledgements**

447

448    **Author Contributions**

449    J.L.R.A and A.W.P conceived the project; K.L.V., D.W., B.C., D.T., V.T., and

450    A.J.S. performed the experiments; K.L.V., B.C., R.R., A.J.S., J.L.R.A. and

451    A.W.P. discussed the results; K.L.V. and J.L.R.A. wrote the manuscript.

452

453

454 **Supporting Information**

455 PISA analysis, detailed AUC data, structural models and additional SAXS data

456 including single value decomposition, calculated P(r) distributions, OLIGOMER

457 models, ABfr dissociation data and background subtraction examples are provided in

458 the supporting information.

## References

459

460    1.    Bhaskar, S. & Lim, S. Engineering protein nanocages as carriers for biomedical

461            applications. *NPG Asia Materials* **9**, e371–e371 (2017).

462    2.    Kanekiyo, M. *et al.* Self-assembling influenza nanoparticle vaccines elicit

463            broadly neutralizing H1N1 antibodies. *Nature* **499**, 102–106 (2013).

464    3.    Ren, H., Zhu, S. & Zheng, G. Nanoreactor design based on self-assembling

465            protein nanocages. *Int. J. Mol. Sci.* **20**, (2019).

466    4.    Maity, B., Fujita, K. & Ueno, T. Use of the confined spaces of apo-ferritin and

467            virus capsids as nanoreactors for catalytic reactions. *Curr. Opin. Chem. Biol.* **25**,

468            88–97 (2015).

469    5.    Douglas, T. & Stark, V. T. Nanophase cobalt oxyhydroxide mineral synthesized

470            within the protein cage of ferritin. *Inorg. Chem.* **39**, 1828–1830 (2000).

471    6.    Yamashita, I., Hayashi, J. & Hara, M. Bio-template Synthesis of Uniform CdSe

472            Nanoparticles Using Cage-shaped Protein, Apoferritin. *Chem. Lett.* **33**, 1158–

473            1159 (2004).

474    7.    Ueno, T. *et al.* Size-selective olefin hydrogenation by a Pd nanocluster provided

475            in an apo-ferritin cage. *Angew. Chemie - Int. Ed.* **43**, 2527–2530 (2004).

476    8.    Douglas, T. *et al.* Protein engineering of a viral cage for constrained

477            nanomaterials synthesis. *Adv. Mater.* **14**, 415–418 (2002).

478    9.    He, D. & Marles-Wright, J. Ferritin family proteins and their use in

479            bionanotechnology. *N. Biotechnol.* **32**, 651–657 (2015).

480   10.    Jutz, G., Van Rijn, P., Santos Miranda, B. & Böker, A. Ferritin: A versatile

481            building block for bionanotechnology. *Chem. Rev.* **115**, 1653–1701 (2015).

482   11.    Putri, R. M. *et al.* Structural Characterization of Native and Modified Encapsulins

483            as Nanoplatforms for in Vitro Catalysis and Cellular Uptake. *ACS Nano* **11**,

484    12796–12804 (2017).

485    12.   Choi, S. H., Kwon, I. C., Hwang, K. Y., Kim, I. S. & Ahn, H. J. Small heat shock

486          protein as a multifunctional scaffold: Integrated tumor targeting and caspase

487          imaging within a single cage. *Biomacromolecules* **12**, 3099–3106 (2011).

488    13.   Azuma, Y., Edwardson, T. G. W. & Hilvert, D. Tailoring lumazine synthase

489          assemblies for bionanotechnology. *Chemical Society Reviews* **47**, 3543–3557

490          (2018).

491    14.   Butterfield, G. L. *et al.* Evolution of a designed protein assembly encapsulating

492          its own RNA genome. *Nature* **552**, 415–420 (2017).

493    15.   Malay, A. D. *et al.* An ultra-stable gold-coordinated protein cage displaying

494          reversible assembly. *Nature* **569**, 438–442 (2019).

495    16.   Swift, J., Butts, C. A., Cheung-Lau, J., Yerubandi, V. & Dmochowski, I. J.

496          Efficient Self-Assembly of Archaeoglobus fulgidus ferritin around metallic cores.

497          *Langmuir* **25**, 5219–5225 (2009).

498    17.   Sana, B., Johnson, E. & Lim, S. The unique self-assembly/disassembly property

499          of Archaeoglobus fulgidus ferritin and its implications on molecular release from

500          the protein cage. *Biochim. Biophys. Acta - Gen. Subj.* **1850**, 2544–2551 (2015).

501    18.   Nasrollahi, F. *et al.* Incorporation of Graphene Quantum Dots, Iron, and

502          Doxorubicin in/on Ferritin Nanocages for Bimodal Imaging and Drug Delivery.

503          *Adv. Ther.* **3**, 1900183 (2020).

504    19.   Fletcher, J. M. *et al.* Self-assembling cages from coiled-coil peptide modules.

505          *Science (80-. ).* **340**, 595–599 (2013).

506    20.   Peng, T. & Lim, S. Trimer-based design of pH-responsive protein cage results

507          in soluble disassembled structures. *Biomacromolecules* **12**, 3131–3138 (2011).

508    21.   Dalmau, M., Lim, S. & Wang, S. W. Design of a pH-dependent molecular switch

509       in a caged protein platform. *Nano Lett.* **9**, 160–166 (2009).

510  22.  Pontillo, N., Pane, F., Messori, L., Amoresano, A. & Merlino, A. Cisplatin

511       encapsulation within a ferritin nanocage: A high-resolution crystallographic

512       study. *Chem. Commun.* **52**, 4136–4139 (2016).

513  23.  Liu, X. *et al.* Apoferritin-CeO2nano-truffle that has excellent artificial redox

514       enzyme activity. *Chem. Commun.* **48**, 3155–3157 (2012).

515  24.  Skouri-Panet, F., Quevillon-Cheruel, S., Michiel, M., Tardieu, A. & Finet, S.

516       sHSPs under temperature and pressure: The opposite behaviour of lens alpha-

517       crystallins and yeast HSP26. *Biochim. Biophys. Acta - Proteins Proteomics*

518       **1764**, 372–383 (2006).

519  25.  White, H. E. *et al.* Multiple Distinct Assemblies Reveal Conformational Flexibility

520       in the Small Heat Shock Protein Hsp26. *Structure* **14**, 1197–1204 (2006).

521  26.  Zhang, T. *et al.* Effect of high hydrostatic pressure (HHP) on structure and

522       activity of phytoferritin. *Food Chem.* **130**, 273–278 (2012).

523  27.  Wang, Q. *et al.* High hydrostatic pressure encapsulation of doxorubicin in ferritin

524       nanocages with enhanced efficiency. *J. Biotechnol.* **254**, 34–42 (2017).

525  28.  Brooks, N. J. *et al.* Automated high pressure cell for pressure jump x-ray

526       diffraction. *Rev. Sci. Instrum.* **81**, 064103 (2010).

527  29.  Svergun, D., Barberato, C. & Koch, M. H. CRYSOL - A program to evaluate X-

528       ray solution scattering of biological macromolecules from atomic coordinates. *J.*

529       *Appl. Crystallogr.* **28**, 768–773 (1995).

530  30.  Konarev, P. V., Volkov, V. V., Sokolova, A. V., Koch, M. H. J. & Svergun, D. I.

531       PRIMUS: A Windows PC-based system for small-angle scattering data analysis.

532       *J. Appl. Crystallogr.* **36**, 1277–1282 (2003).

533  31.  Krissinel, E. & Henrick, K. Inference of Macromolecular Assemblies from

534    Crystalline State. *J. Mol. Biol.* **372**, 774–797 (2007).

535    32.    Stefanini, S., Vecchini, P. & Chiancone, E. On the Mechanism of Horse Spleen

536    Apoferritin Assembly: A Sedimentation Velocity and Circular Dichroism Study.

537    *Biochemistry* **26**, 1831–1837 (1987).

538    33.    Gerl, M. & Jaenicke, R. Mechanism of the self-assembly of apoferritin from horse

539    spleen - Cross-linking and spectroscopic analysis. *Eur. Biophys. J.* **15**, 103–109

540    (1987).

541    34.    Banyard, S. H., Stammers, D. K. & Harrison, P. M. Electron density map of

542    apoferritin at 2.8-Å resolution. *Nature* **271**, 282–284 (1978).

543    35.    Sato, D. *et al.* Ferritin Assembly Revisited: A Time-Resolved Small-Angle X-ray

544    Scattering Study. *Biochemistry* **55**, 287–293 (2016).

545    36.    Kilic, M. a, Spiro, S. & Moore, G. R. Stability of a 24-meric homopolymer:

546    comparative studies of assembly-defective mutants of Rhodobacter capsulatus

547    bacterioferritin and the native protein. *Protein Sci.* **12**, 1663–1674 (2003).

548    37.    Andrews, S. C. *et al.* Physical, chemical and immunological properties of the

549    bacterioferritins of Escherichia coli, Pseudomonas aeruginosa and Azotobacter

550    vinelandii. *Biochim. Biophys. Acta - Protein Struct. Mol. Enzymol.* **1078**, 111–

551    116 (1991).

552    38.    Wiedemann, C., Bellstedt, P. & Görlach, M. CAPITO - A web server-based

553    analysis and plotting tool for circular dichroism data. *Bioinformatics* **29**, 1750–

554    1757 (2013).

555    39.    Weber, G. Thermodynamics of the association and the pressure dissociation of

556    oligomeric proteins. *J. Phys. Chem.* **97**, 7108–7115 (1993).

557    40.    Atkins, P. & de, P. J. Atkins' Physical Chemistry, 7th Edition. *Oxford Univ. Press*

558    (2002).

559    41.    Ward, A. B., Sali, A. & Wilson, I. A. Integrative Structural Biology. *Science (80-.*

560            *).* **339**, 913–915 (2013).

561    42.    Brooks-Bartlett, J. C. *et al.* Development of tools to automate quantitative

562            analysis of radiation damage in SAXS experiments. *J. Synchrotron Radiat.* **24**,

563            63–72 (2017).

564    43.    Kikhney, A. G. & Svergun, D. I. A practical guide to small angle X-ray scattering

565            (SAXS) of flexible and intrinsically disordered proteins. *FEBS Lett.* **589**, 2570–

566            2577 (2015).

567    44.    Sato, D. *et al.* Electrostatic Repulsion during Ferritin Assembly and Its Screening

568            by Ions. *Biochemistry* **55**, 482–488 (2016).

569    45.    Watt, R. K., Hilton, R. J. & Graff, D. M. Oxido-reduction is not the only

570            mechanism allowing ions to traverse the ferritin protein shell. *Biochimica et*

571            *Biophysica Acta - General Subjects* **1800**, 745–759 (2010).

572    46.    Bakker, G. R. & Boyer, R. F. Iron incorporation into apoferritin. The role of

573            apoferritin as a ferroxidase. *J. Biol. Chem.* **261**, 13182–13185 (1986).

574    47.    Rui, H., Rivera, M. & Im, W. Protein dynamics and ion traffic in bacterioferritin.

575            *Biochemistry* **51**, 9900–9910 (2012).

576    48.    Kegel, W. K. & van der Schoot, P. Competing Hydrophobic and Screened-

577            Coulomb Interactions in Hepatitis B Virus Capsid Assembly. *Biophys. J.* **86**,

578            3905–3913 (2004).

579    49.    Silva, J. Pressure Stability of Proteins. *Annu. Rev. Phys. Chem.* **44**, 89–113

580            (1993).

581    50.    Silva, J. L., Foguel, D. & Royer, C. A. Pressure provides new insights into protein

582            folding, dynamics and structure. *Trends Biochem. Sci.* **26**, 612–618 (2001).

583    51.    Silva, J. L. & Weber, G. Pressure-induced dissociation of brome mosaic virus.

584       *J. Mol. Biol.* **199**, 149–159 (1988).

585   52.   Leimkühler, M., Goldbeck, A., Lechner, M. D. & Witz, J. Conformational changes

586       preceding decapsidation of bromegrass mosaic virus under hydrostatic

587       pressure: A small-angle neutron scattering study. *J. Mol. Biol.* **296**, 1295–1305

588       (2000).

589   53.   Leimkühler, M. *et al.* The formation of empty shells upon pressure induced

590       decapsidation of turnip yellow mosaic virus. *Arch. Virol.* **146**, 653–667 (2001).

591   54.   Teale, F. W. J. Cleavage of the haem-protein link by acid methylethylketone.

592       *BBA - Biochim. Biophys. Acta* **35**, 543 (1959).

593   55.   Nayuk, R. & Klaus, H. Formfactors of Hollow and Massive Rectangular

594       Parallelepipeds at Variable Degree of Anisometry. *Zeitschrift für Physikalische*

595       *Chemie* **226**, 837 (2012).

596   56.   Willies, S. C., Isupov, M. N., Garman, E. F. & Littlechild, J. A. The binding of

597       haem and zinc in the 1.9 Å X-ray structure of Escherichia coli bacterioferritin. *J.*

598       *Biol. Inorg. Chem.* **14**, 201–207 (2009).

599   57.   Hingorani, K. *et al.* Photo-oxidation of tyrosine in a bio-engineered

600       bacterioferritin 'reaction centre' - A protein model for artificial photosynthesis.

601       *Biochim. Biophys. Acta - Bioenerg.* **1837**, 1821–1834 (2014).

602   58.   Ardejani, M. S., Li, N. X. & Orner, B. P. Stabilization of a protein nanocage

603       through the plugging of a protein-protein interfacial water pocket. *Biochemistry*

604       **50**, 4029–4037 (2011).

605   59.   Wong, S. G. *et al.* Structural and mechanistic studies of a stabilized subunit

606       dimer variant of Escherichia coli bacterioferritin identify residues required for

607       core formation. *J. Biol. Chem.* **284**, 18873–18881 (2009).

608   60.   Fan, R., Boyle, A. L., Vee, V. C., See, L. N. & Orner, B. P. A helix swapping

609    study of two protein cages. *Biochemistry* **48**, 5623–5630 (2009).

610  61.  Hargrove, M. S. *et al.* Stability of Myoglobin: A Model for the Folding of Heme

611    Proteins. *Biochemistry* **33**, 11767–11775 (1994).

612  62.  Andrews, S. C. *et al.* Overproduction, purification and characterization of the

613    bacterioferritin of Escherichia coli and a C-terminally extended variant. *Eur. J.*

614    *Biochem.* **213**, 329–338 (1993).

615  63.  Basham, M. *et al.* Data Analysis WorkbeNch (DAWN). *J. Synchrotron Radiat.*

616    **22**, 853–858 (2015).

617  64.  Hussain, R., Jávorfi, T. & Siligardi, G. Circular dichroism beamline B23 at the

618    Diamond Light Source. *J. Synchrotron Radiat.* **19**, 132–135 (2012).

619  65.  De Val, N., Declercq, J. P., Lim, C. K. & Crichton, R. R. Structural analysis of

620    haemin demetallation by L-chain apoferritins. *J. Inorg. Biochem.* **112**, 77–84

621    (2012).

622  66.  Chen, C. R. & Makhatadze, G. I. ProteinVolume: calculating molecular van der

623    Waals and void volumes in proteins. *BMC Bioinformatics* **16**, 101 (2015).

624  67.  Demeler, B. *et al.* Characterization of size, anisotropy, and density heterogeneity

625    of nanoparticles by sedimentation velocity. *Anal. Chem.* **86**, 7688–7695 (2014).

626  68.  Wald, A. & Wolfowitz, J. On a Test Whether Two Samples are from the Same

627    Population. *Ann. Math. Stat.* **11**, 147–162 (1940).

628  69.  Hansen, S. BayesApp: A web site for indirect transformation of small-angle

629    scattering data. *J. Appl. Crystallogr.* **45**, 566–567 (2012).

630

631
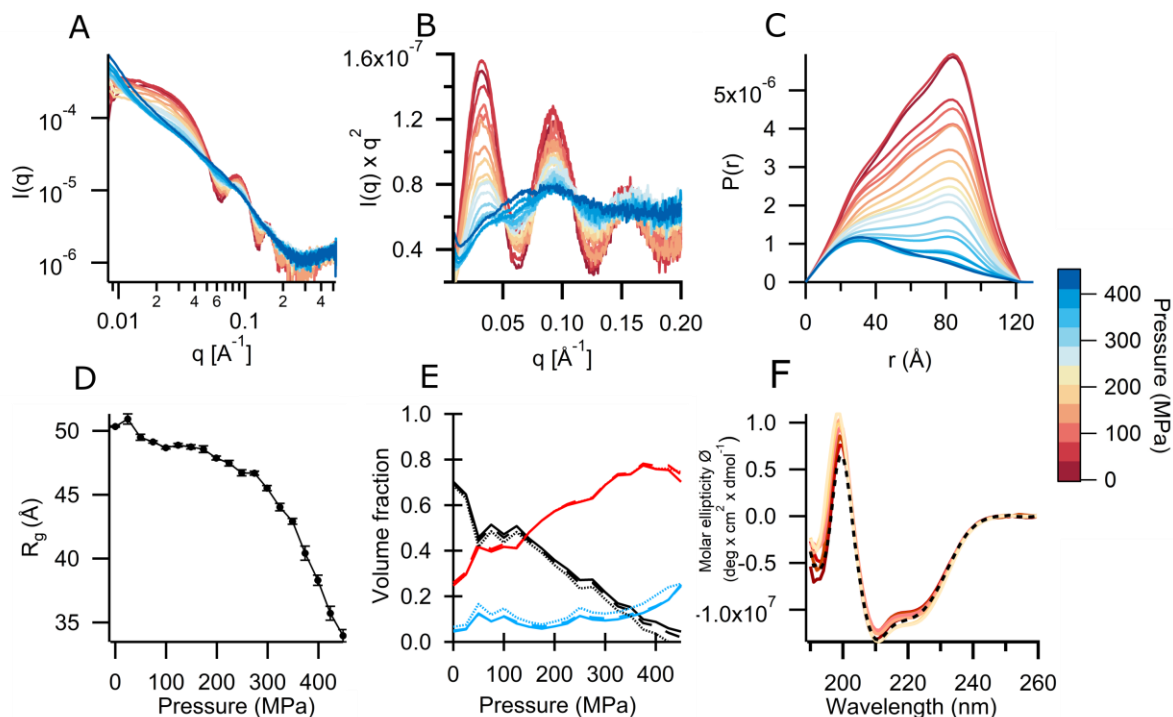
**Figure 1. Pressure dissociation of ABfr under equilibrium conditions between 0.1 and 450 MPa measured using high pressure synchrotron radiation SAXS and circular dichroism. (A)** Reciprocal space SAXS profiles, **(B)** Kratky plots, **(C)** pair distance distribution (P(r)) functions, **(D)** change in radius of gyration, $R_g$, with pressure, **(E)** change in solution oligomer composition with pressure and **(F)** circular dichroism spectra. SAXS data were collected between 0.1 MP (red) and 450 MPa (blue) at a protein concentration of 5 mg mL$^{-1}$ in 45 mM sodium phosphate buffer (pH 7). Real space transformations were performed using BAYESAPP, which uses Bayesian analysis to select parameters such as $D_{max}$ and data noise level.[69] I(0) and $R_g$ were calculated from real space data. I(0) was normalised to a maximum value of 1. Component volume fraction versus pressure generated from OLIGOMER models of ABfr dissociation. The volume fractions of the icositetramer, *n*-mer and dimer are shown in black, blue and red respectively. The intermediate oligomer states are hexamer (solid line), octamer (dashed line) and dodecamer (dotted line). High-pressure circular dichroism data was collected between 0.1 (red) and 200 MPa (yellow) at a protein concentration of 0.03 mg mL$^{-1}$, 45 mM sodium phosphate, pH 7.
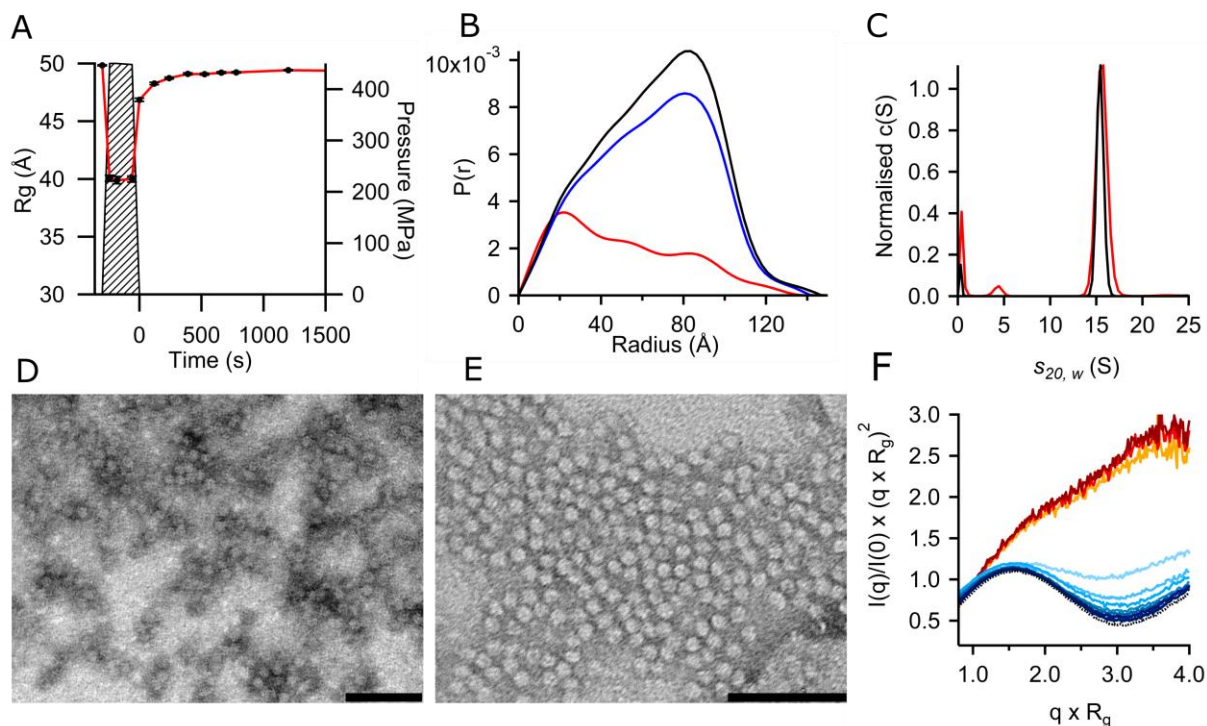
662
663 **Figure 2. Reassociation of ABfr following pressure induced dissociation measured by SAXS,**
664 **AUC and TEM. (A)** Changes in ABfr $R_g$ pre, during and post- pressurization measured by SAXS.
665 Pressure cycle was performed at 25°C NaPi (45 mM, pH 7, I = 123 mM). **(B)** Pair distance distribution
666 (P(r)) functions for ABfr pre- (black), during (red) and post- pressurisation (blue). **(C)** Sedimentation
667 velocity c(S) distribution for ABfr pre-pressurisation (black) and post-pressurisation (red). Sedimentation
668 velocity was measured at a protein concentration of approximately 50 µM in sodium phosphate buffer
669 (45 mM NaPi, 250 mM NaCl, pH 7) using a Beckmann ProteomeLab XL-I at 20°C and 24000 rpm. Data
670 was collected at a wavelength of 418 nm. Data file time stamps were corrected using REDATE, and
671 continuous sedimentation coefficient (c(S)) distributions were fitted using SEDFIT. Buffer density (ρ =
672 1.003 g cm-3) and viscosity (η = 1.0107 mPa s-1) were measured using an Anton-Paar rolling ball
673 viscometer. **(D)** Negative stain (phosphotungstic acid) TEM images of ABfr pre-pressurisation and **(E)**
674 and post-pressurisation (scale bars = 100 nm). **(F)** Change in normalised Kratky intensity
675 ($I_{(q=1.1)}/I_{(0)}$x$(q*R_g)^2$) with pre, during and post- pressurization. Dotted black trace shows pre-
676 pressurisation data, yellow – red traces show pressurised data at 0, 120 and 300s, light blue – dark
677 blue traces show post pressurisation data with increasing time.
678
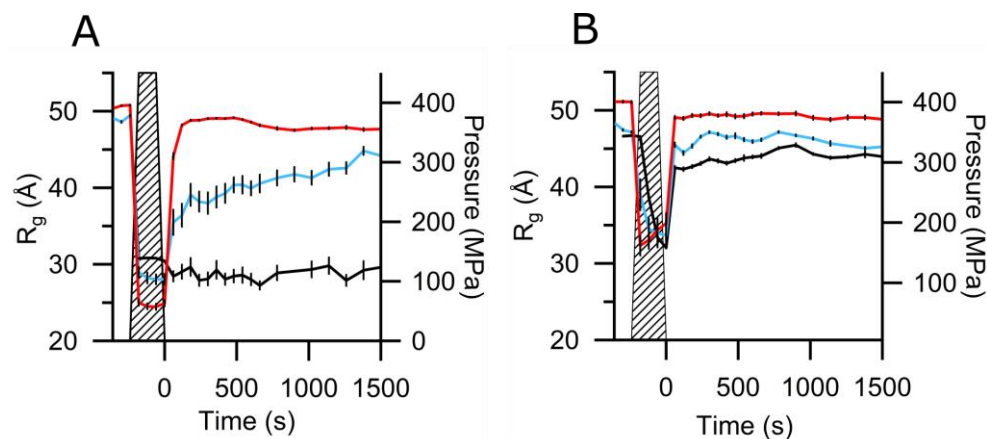
**Figure 3. Changes in ABfr $R_g$ pre, during and post- pressurisation.** Pressure cycles were performed at 5 °C **(A)** and 25°C **(B)** in $H_2O$ (I = 0 mM, black), NaPi (45 mM, pH 7, I = 123 mM, blue) and in NaPi (45 mM, pH 7) + NaCl (250 mM) (I = 373 mM, red). Pressure level depicted as hashed region.

684
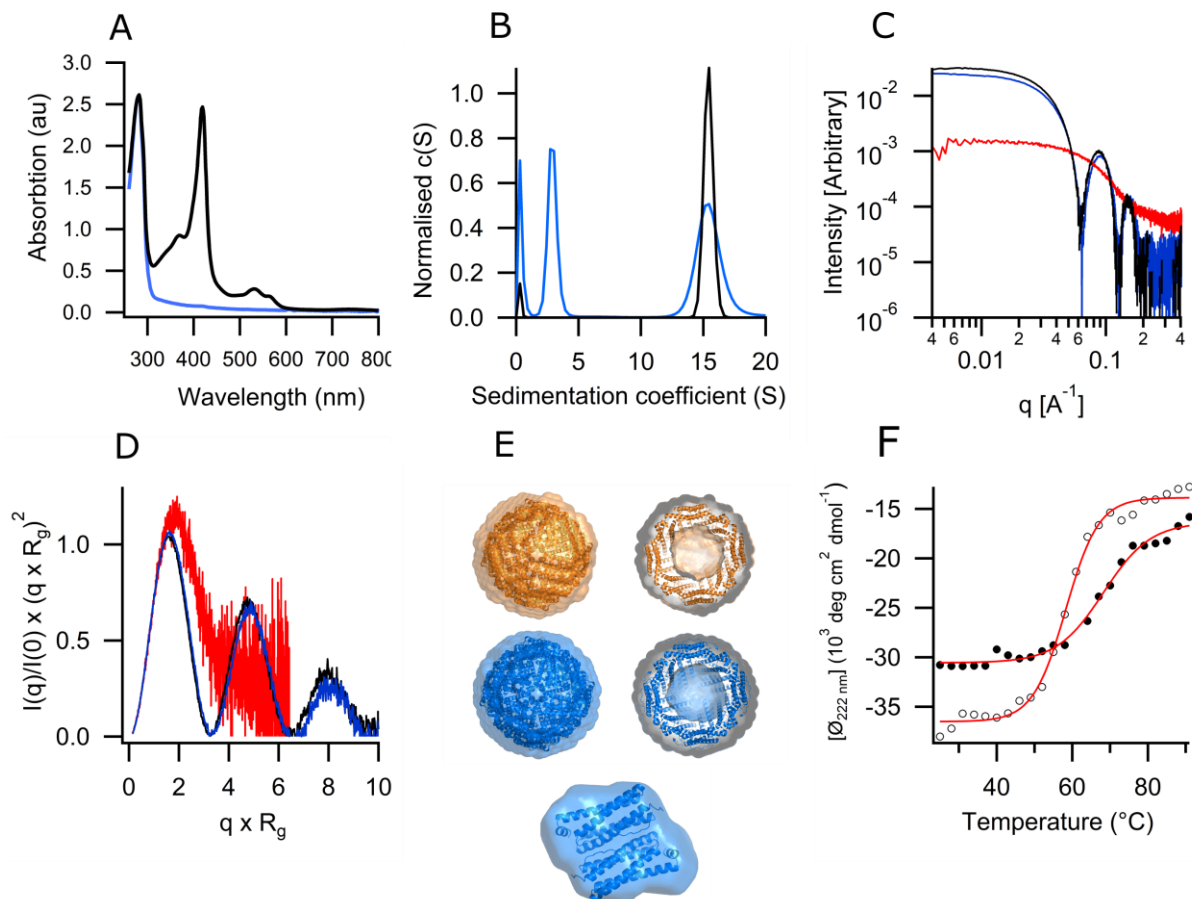


685
**Figure 4. Physicochemical characterization of ABfr and AABfr under ambient pressure. (A)** UV/visible spectra of ABfr (black) and AABfr (blue). UV-visible spectra were recorded measured at a protein concentration of approximately 50 µM in sodium phosphate buffer (45 mM NaPi, 250 mM NaCl, pH 7). Curves are normalised to A280 = 1 to highlight differences in heme absorbance. **(B)** SV-AUC c(s) distributions for ABfr (black) and AABR (blue). Sedimentation velocity was measured at a protein concentration of approximately 50 µM in potassium phosphate buffer (45 mM KPi, 250 mM NaCl, pH 7) using a Beckmann ProteomeLab XL-I at 20˚C and 24000 rpm. Data was collected at a wavelength of 280 nm. Data file time stamps were corrected using REDATE, and continuous sedimentation coefficient (c(S)) distributions were fitted using SEDFIT. Buffer density ($\rho$ = 1.003 g cm$^{-3}$) and viscosity ($\eta$ = 1.0107 mPa 865-) were measured using an Anton-Paar rolling ball viscometer. The protein partial specific volume was calculated from the primary sequence ($\tilde{v}$ = 0.736 cm$^3$ g$^{-1}$). **(C)** HPLC-SAXS profiles and **(D)** Kratky plots for ABfr icositetramer (black) and AABfr icositetramer (blue) and dimer (red). **(E)** *Ab initio* bead model of ABfr (icositetramer, orange) and AABfr (icositetramer and dimer, blue), overlaid with corresponding crystal structures (2VXI and 4CVP)[56,57]. Real space transformations were performed using ScÅtter. The maximum diameter was determined by selecting values that resulted in high reciprocal fit quality, and produced smooth, oscillation-free, real-space functions that decreased smoothly to zero at high radius. A constant background was applied in the transformation, and real space distributions were refined using the L1 norm of the Moore coefficients as a regularisation target.The *ab initio* models were produced from refined pair distance distribution functions using DAMMIF, and are DAMAVER averages of 23 runs. The models and crystal structures were visualized using PyMOL. **(F)** Thermal denaturation far-UV circular dichroism spectra and fits for ABfr (open circles) and AABfr (black circles). Data were collected at B23, Diamond Light Source, UK. Measurements were performed in potassium phosphate buffer (45 mM, pH 7) at a protein concetnration of 0.5 g L$^{-1}$. Raw data was converted to mean residue elipticity and secondary structure analysis was performed using CAPITO.

715
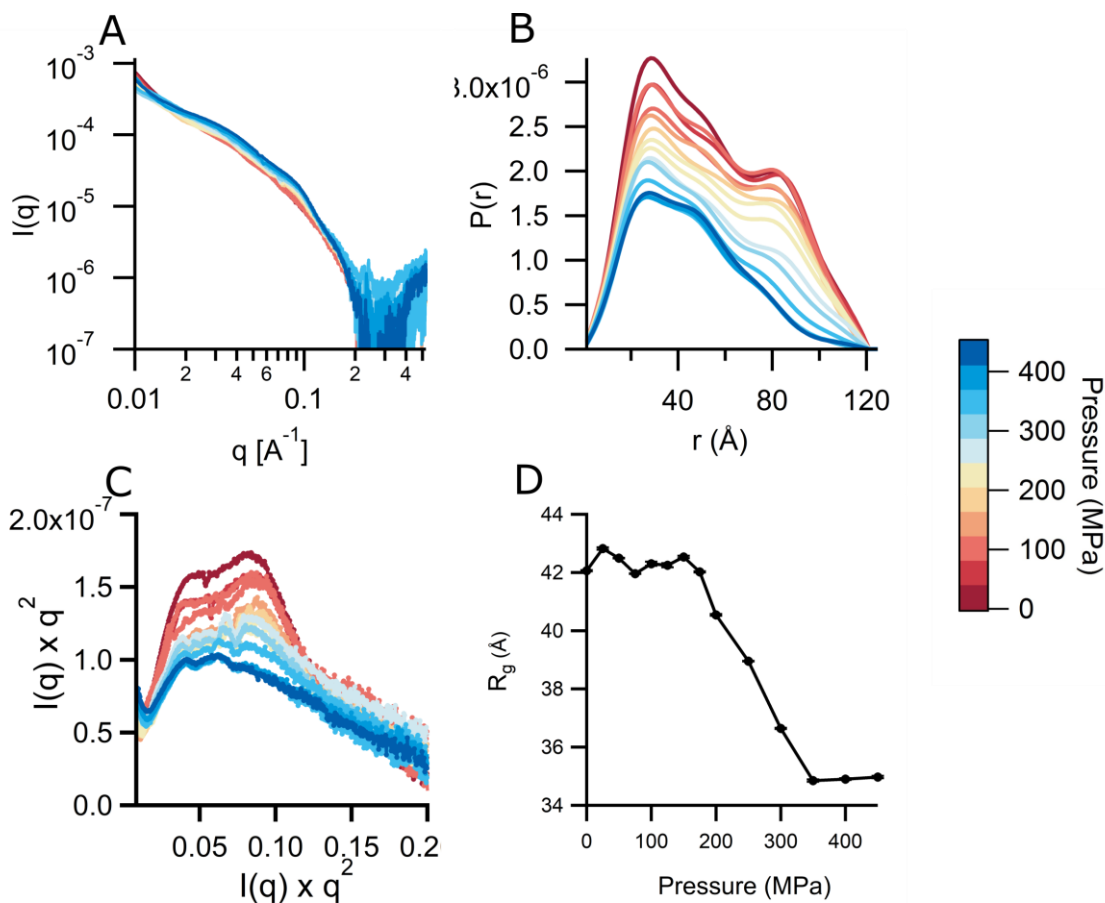
**Figure 5. Pressure dissociation of AABfr under equilibrium conditions between 0.1 and 450 MPa.**
**(A)** reciprocal space SAXS profiles, **(B)** Pair distance distribution (P(r)) functions, **(C)** Kratky plots and
**(D)** Radius of gyration, $R_g$. SAXS data was collected between 0.1 MP (red) and 450 MPa (blue) at a
protein concentration of 5 mg mL$^{-1}$ in 45 mM sodium phosphate buffer (pH 7). Real space
transformations were performed using BAYESAPP, which uses Bayesian analysis to select parameters
such as $D_{max}$ and data noise level.[69] I(0) and $R_g$ were calculated from real space data. I(0) was
normalised to a maximum value of 1.

723